Otopro Volume 22 No. 1 Nov 2026 pages. 9-16
P-ISSN: 1858-411x; E-ISSN: 2685-7863
DOI: 10.26740/otopro.v22n1.p9-16 https://journal.unesa.ac.id/index.php/jo
(This journal accommodates review, experimental, and thinking related to mechanical engineering and its application)

THE EFFECT OF VARIATIONS IN CURRENT AND WELDING SPEED OF SMAW ON THE MECHANICAL PROPERTIES AND MICROSTRUCTURE OF LOW CARBON STEEL

Yudi Siswanto[1*], *Angga* Tegar Setiawan[2], *Amiruddin*[3], *and Ika* Nurjannah[4]
[123] Program Studi Teknik Perawatan Mesin, Politeknik Industri Logam Morowali, Morowali, Indonesia
yudi@pilm.ac.id
[4] Teknik Mesin, Fakultas Teknik, Universitas Negeri Surabaya, Surabaya, Indonesia
ikajannah@unesa.ac.id

Abstract. Shielded metal arc welding (SMAW) of SS400 low-carbon steel was evaluated using a 3² full-factorial design with welding currents of 70, 80 and 90 A and travel speeds of 2, 3 and 4 mm/s (three replicates per setting; n = 27). Heat input was recalculated with consistent units, using a nominal arc voltage of 25 V and assumed thermal efficiency of 0.83. The resulting nominal heat-input range was 0.363–0.934 kJ/mm. The highest mean ultimate tensile strength (UTS, 439.2 MPa) and heat-affected-zone (HAZ) hardness (187.0 HV) were obtained at 70 A/4 mm/s, compared with the lowest corresponding values of 385.8 MPa and 158.0 HV at 90 A/2 mm/s. The author-supplied microstructural measurements showed a smaller mean HAZ grain size under the lower-input condition (13.7 ± 2.4 µm versus 20.3 ± 3.1 µm; five fields per condition). Two-way ANOVA of the 27 individual test records identified effects of current (UTS $p = 0.0118$; hardness $p = 0.00229$) and travel speed (UTS $p = 0.00136$; hardness $p = 0.000027$), with no detected interaction. An additive regression gave $UTS = 459.583 - 1.05833I + 13.78333v$ ($R^2 = 0.590$). Residual non-normality limits the strength of the inferential claims. These findings establish the best observed welding setting within the tested experimental range and provide a transparent basis for further qualification.

Keywords: SMAW; low-carbon steel; welding current; travel speed; heat input; tensile strength; HAZ hardness; grain size

1 Introduction

Welding is one of the most widely employed metal-joining processes in manufacturing, structural construction, and industrial maintenance [1]. Among various welding techniques, Shielded Metal Arc Welding (SMAW) remains prominent due to its operational flexibility, portability, and relatively low equipment cost [2]. The SMAW process involves the generation of an electric arc between a flux-coated consumable electrode and the base metal, producing localised melting and subsequent solidification that forms the weld joint [3]. The flux coating generates a protective slag and shielding gases that prevent atmospheric contamination of the weld pool, stabilise the arc, and contribute to the chemical composition of the deposited metal [4].

Among the controllable SMAW variables, welding current (I) and travel speed (v) jointly influence arc energy per unit weld length. For speed stated in mm/s, nominal effective heat input is calculated as $\eta VI/(1000v)$ in kJ/mm, where η denotes assumed process thermal efficiency and V denotes voltage [5]. The thermal cycle can modify the weld metal (WM), fusion boundary (FB), and heat-affected zone (HAZ), influencing tensile behaviour and hardness [6].

SS400 low-carbon structural steel is widely used in fabrication because of its formability and weldability

*Coresponding author: yudi@pilm.ac.id

[7,21]. Its ferritic–pearlitic microstructure may respond to welding thermal cycles through local changes in grain morphology and phase distribution. The relationship between the selected welding conditions and mechanical response must therefore be evaluated with consistent units and traceable experimental evidence, without inferring an unmeasured cooling rate or phase fraction.

Prior studies have examined SMAW parameters, steel-joint mechanical properties and metallurgical features [9–13,21]. Nevertheless, comparisons may be difficult when operating conditions, heat-input definitions and measured properties are reported separately. The present manuscript specifically assesses concurrent variations in current and speed in nine SS400 welding conditions and aligns the resulting heat-input calculations with the reported tensile, hardness and micrograph observations. Claims of first-in-field novelty are not made.

The contribution of this work is the integration of a replicated 3×3 SMAW factorial design with dimensionally consistent nominal heat-input calculations, tensile and HAZ-hardness observations, quantitative HAZ grain-size summaries supplied with the photomicrographs, and specimen-level ANOVA and regression. The study reports both the best observed settings and the limitations of statistical model assumptions, rather than claiming universal process optimisation.

2 Literature review

2.1 SMAW Process and Heat Input

SMAW produces a coalescent bond by melting the base material and electrode tip through resistive and convective heat transfer from the electric arc [4]. The thermal energy deposited per unit weld length—heat input—is calculated according to the standard expression:

$$HI = (\eta \times V \times I)/(1000 \times v) \quad [\text{kJ/mm}], \text{ with v inmm/s.} \quad (1)$$

In Equation (1), V is arc voltage (V), I is current (A), v is travel speed (mm/s), and η is the assumed dimensionless thermal efficiency. The factor 60 is not included when speed is expressed in mm/s; 1 V × 1 A = 1 J/s, so the quotient yields J/mm and division by 1000 yields kJ/mm. The nominal value η = 0.83 is retained from the experimental calculations, while 0.80 is cited as a comparison factor for manual metal arc welding [26].

Cooling through approximately 800–500 °C is often discussed using the $t_{8/5}$ cooling-time descriptor [6,8]. The present work did not measure $t_{8/5}$. Therefore, links between nominal heat input and observed micrographs are interpreted as metallurgically plausible associations rather than direct measurements of cooling rate, local phase fraction or hardening mechanism. E6013 (AWS A5.1) is a rutile-coated SMAW electrode; its coating should not be characterised as a low-hydrogen system without supporting diffusible-hydrogen testing [13].

2.2 Mechanical Properties of Welded Joints

A transverse welded-joint tensile result reflects the load-bearing response of the whole joint and may be affected by defects, local microstructure and fracture location. The Hall–Petch concept relates grain size to yield strength under specified conditions; it should not be used here to calculate a numerical Vickers-hardness difference without fitted material-specific coefficients [8,14]. HAZ Vickers indentations offer a local hardness comparison, provided that indentation position, load and replicate variation are documented [15].

Published work suggests that welding current and travel speed influence heat input, bead geometry and local mechanical behaviour, but the direction and magnitude of their effects depend on material, joint configuration and welding quality [9,10,16,17]. The present study therefore compares the nine observed factorial conditions directly; it does not assume that every increase in speed must produce a monotonic increase in UTS.

2.3 Statistical Analysis in Welding Research

Two-way fixed-factor ANOVA partitions 27 replicate-level outcomes into current (2 df), speed (2 df), current × speed interaction (4 df), and within-cell error (18 df) [18,19]. The residual distributions and variance homogeneity should be checked before interpreting nominal F-tests. Separately, an additive OLS equation in current and speed can describe within-design UTS associations; predictions must be assessed using the same 27 observed specimen results rather than only the nine group means.

Park et al. [20] provide an example of regression and machine learning for weld-related mechanical properties in a different alloy system. In the present SS400 study, multiple regression is restricted to current and travel speed; calculated nominal heat input is not introduced simultaneously as a separate predictor because it is constructed from the same variables at fixed voltage and efficiency.

3 Materials and methods

3.1 Base Material and Electrode

SS400 low-carbon steel plates (JIS G3101) with a nominal thickness of 6 mm were used as the base material. Before welding, plate coupons measured 200×100 mm and were cleaned and ground to remove surface contamination. The reported consumable was an E6013 electrode (AWS A5.1) of 3.2 mm diameter, conditioned at 150 °C for 2 h before use. These plate-coupon dimensions should not be confused with the machined tensile specimen gauge section.

3.2 Welding Equipment and Procedure

Welding was carried out using a 200 A SMAW inverter (MMA-200) in direct-current electrode-positive (DCEP) mode, with a nominal arc voltage of 25 ± 2 V. A single-pass V-groove joint, 45° groove angle and 2 mm root gap were used. The effective heat input is an estimate calculated at the nominal 25 V and $\eta = 0.83$ rather than a directly logged arc-energy measurement. As a reference, the commonly used thermal-efficiency factor for manual metal arc welding is $\eta = 0.80$ [26], and ISO 18491:2026 describes the parameters needed for arc-energy measurement [27].

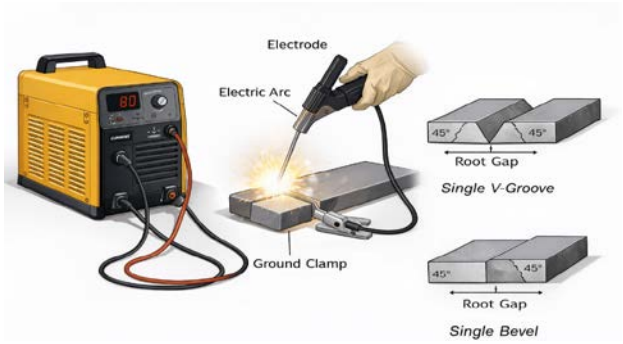


Fig. 1. SMAW welding process schematic and V-groove joint configuration.

Travel speed was controlled by a motorised slide assembly, with nominal repeatability of ±0.1 mm/s and a 100 mm weld length. Ambient temperature was approximately 22 ± 2 °C, and no preheating was applied. Because plate-specific chemical-composition records are not reproduced, no numeric carbon-equivalent value or universal preheating threshold is asserted.

3.3 Experimental Design

A 3^2 full-factorial design was used, comprising three current levels and three travel-speed levels, with three specimens per combination (n = 27). The specimen-level UTS and HAZ-hardness values were retained under individual identifiers S01–S27. Means and sample standard deviations were calculated from each group of three independent test records.

- Current (I): 70, 80, 90 A
- Travel speed (v): 2, 3, 4 mm/s

Nominal effective heat input was evaluated with Equation (1), V = 25 V, $\eta = 0.83$ and speeds in mm/s, giving 0.363–0.934 kJ/mm. If $\eta = 0.80$ is assumed instead, the corresponding range is 0.350–0.900 kJ/mm. For a possible arc voltage of 23–27 V and $\eta = 0.83$, the extreme calculated values span approximately 0.334–1.008 kJ/mm. These are sensitivity scenarios, not measurements of actual arc-energy fluctuation.

3.4 Quality Inspection

Visual inspection was carried out before destructive testing, supplemented by dye-penetrant inspection. The original procedure cited AWS D1.1 and ASME Section V, Article 6 as methodological references. Only visually acceptable specimens progressed to mechanical characterisation; a shallow undercut was noted at 90 A/4 mm/s. No independent inspection report is reproduced here, so code-compliance claims are not extended beyond the tests described.

3.5 Mechanical Testing

Transverse tensile specimens were machined with a nominal gauge length of 50 mm and gauge width of 12.5 mm, with preparation referenced to AWS B4.0. Tensile testing used a 100 kN universal testing machine and 2 mm/min crosshead speed. Vickers hardness was recorded in the HAZ at 1 kgf load (HV1), using traverses at approximately 1 mm spacing. Figure 2 documents a provided welded specimen before and after tensile testing and identifies the weld metal and HAZ. Tensile-test and hardness results were retained for all 27 specimens.

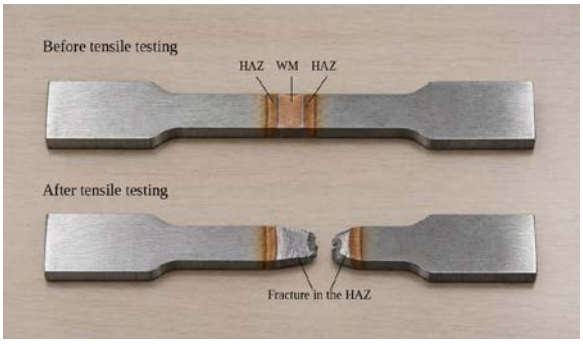


Fig. 2. Welded tensile specimen before and after testing, showing the weld metal (WM), heat-affected zone (HAZ) and fracture region.

The supplied post-test photograph illustrates fracture in the vicinity of the HAZ for the photographed specimen. Its appearance should not be interpreted as evidence that all 27 specimens fractured at that location.

3.6 Microstructural Characterisation

Metallographic sections were cut transverse to the weld axis, mounted, ground using SiC papers up to 1200 grit, polished with 1 µm diamond suspension and etched with 2% nital for 10–15 s. The photomicrographs identify base metal (BM), weld metal (WM), fusion boundary (FB) and heat-affected zone (HAZ). The supplied quantitative annotations report mean grain size ± standard deviation from five fields per condition using a linear-intercept procedure described with reference to ASTM E112 [28]. For the HAZ, the annotated results are 20.3 ± 3.1 µm at 90 A/2 mm/s and 13.7 ± 2.4 µm at 70 A/4 mm/s. These summaries are reproduced as author-supplied measurements; the individual field counts are not tabulated in this article.

Different optical fields and magnifications can affect morphological interpretation. The comparative HAZ

measurements were therefore taken from the supplied image annotations, while constituent identification is described conservatively as predominantly ferrite–pearlite with locally different morphologies.

3.7 Statistical Analysis

For each response (UTS and HAZ hardness), a two-way fixed-factor ANOVA including current, travel speed and their interaction was calculated from the 27 specimen-level values, with residual df = 18 and $\alpha = 0.05$. Sums of squares were partitioned using the balanced 3×3×3 design. Shapiro–Wilk tests on full-model residuals evaluated normality, and a median-centred Levene test across the nine cells evaluated variance homogeneity. Given significant Shapiro–Wilk results, the F-test p-values are reported as nominal exploratory inference rather than definitive evidence satisfying all ANOVA assumptions. A separate additive OLS model for UTS used current (A) and speed (mm/s) as predictors (n = 27); in-sample R^2, adjusted R^2, residual RMSE and residual diagnostics were recomputed. Calculated HI was excluded as a covariate to avoid redundant parameterisation.

All 27 observations were retained in the analysis; no measurements were reconstructed from cell means. ANOVA assumptions were assessed from the full-model residuals, and the fitted regression is explicitly an in-sample descriptive model.

4 Results and discussion

4.1 Heat Input and Experimental Matrix

Table 1 provides the corrected nominal heat-input values and group averages as mean ± sample standard deviation (n = 3). The experimental range is 0.363–0.934 kJ/mm; the previous 32.81–84.38 kJ/mm interval arose from a speed-unit inconsistency and is replaced throughout the manuscript.

Table 1. Welding matrix, corrected nominal heat input and UTS/HAZ hardness as mean ± sample SD (three specimens per cell).

I (A)	v (mm/s)	HI (kJ/mm)	UTS (MPa) mean ± SD	HAZ hardness (HV) mean ± SD
70	2	0.726	421.5 ± 13.3	170.0 ± 5.8
70	3	0.484	419.2 ± 13.2	181.3 ± 5.7
70	4	0.363	439.2 ± 13.3	187.0 ± 5.7
80	2	0.830	400.2 ± 13.2	165.8 ± 5.8
80	3	0.553	419.0 ± 13.3	175.0 ± 5.8
80	4	0.415	430.9 ± 13.2	180.6 ± 5.7
90	2	0.934	385.8 ± 13.3	158.0 ± 5.7
90	3	0.623	410.5 ± 13.3	169.0 ± 5.8
90	4	0.467	420.1 ± 13.3	177.3 ± 5.8

At 70 A/4 mm/s, the highest group means were 439.2 ± 13.3 MPa for UTS and 187.0 ± 5.7 HV for HAZ hardness. At 90 A/2 mm/s, the corresponding minima were 385.8 ± 13.3 MPa and 158.0 ± 5.7 HV. Between these settings, UTS differed by 53.4 MPa (13.8%) and hardness by 29.0 HV (18.4%), correcting the earlier stated 14 HV difference.

4.2 Effect of Heat Input on UTS and HAZ Hardness

Figure 3 presents the 27 individual measurements, together with the nine condition means, against nominal effective heat input. Both UTS and HAZ hardness tend to decrease over the tested combinations as the estimated thermal input increases. The figure uses the observed UTS range of approximately 377–453 MPa rather than the erroneous 230–280 MPa scale previously shown in Figure 6.

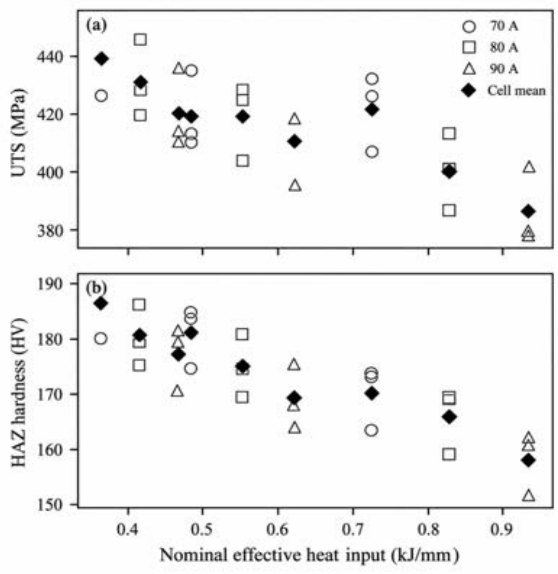


Fig. 3. Measured (a) UTS and (b) HAZ hardness versus corrected nominal effective heat input. Open circles: individual specimen values (n = 27); diamonds: means of the nine welding conditions.

At a fixed 70 A, increasing speed from 2 to 4 mm/s reduced nominal heat input from 0.726 to 0.363 kJ/mm and increased mean UTS from 421.5 to 439.2 MPa (+4.2%) and mean hardness from 170.0 to 187.0 HV (+10.0%). Across all nine conditions the pattern is not perfectly monotonic, so the descriptive trends should not be confused with a deterministic one-variable relation.

4.3 Microstructural Analysis

Figures 4 and 5 present the supplied optical micrographs for the high-input (90 A/2 mm/s) and low-input (70 A/4 mm/s) welding conditions, respectively. Region labels identify BM, WM, FB and HAZ, with phase descriptions and calibrated scale bars retained as provided. The HAZ comparison focuses on the grain-size summaries reported for five fields per condition, rather than treating the range labels of the earlier manuscript as new measurements.

For the highest-input condition (90 A/2 mm/s; nominal HI = 0.934 kJ/mm), Figure 4 shows a relatively coarse HAZ microstructure. The quantitative annotation for the HAZ reports an average grain size of 20.3 ± 3.1 μm (n = 5 fields). The weld metal and fusion-boundary fields exhibit different morphologies, but grain morphology alone does not prove the presence or absence of a particular phase.

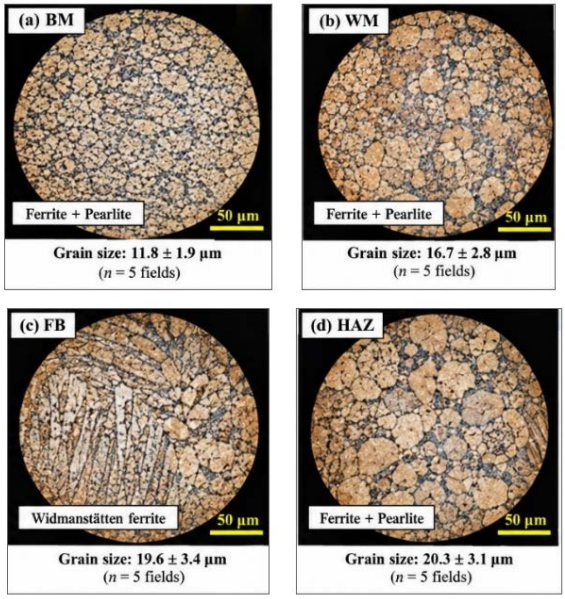


Fig. 4. Optical microstructures of SS400 steel welded at 90 A and 2 mm/s (nominal HI = 0.934 kJ/mm): (a) BM, (b) WM, (c) FB and (d) HAZ. Reported HAZ grain size: 20.3 ± 3.1 μm (n = 5 fields); scale bars are retained from the supplied micrographs.

For the lower-input condition (70 A/4 mm/s; nominal HI = 0.363 kJ/mm), Figure 5 presents a visibly finer HAZ ferrite–pearlite microstructure. The reported mean HAZ grain size is 13.7 ± 2.4 μm (n = 5 fields), approximately 32.5% smaller than the mean at the highest-input condition. This difference is descriptive because the five field-level values and uncertainty propagation are not independently shown here.

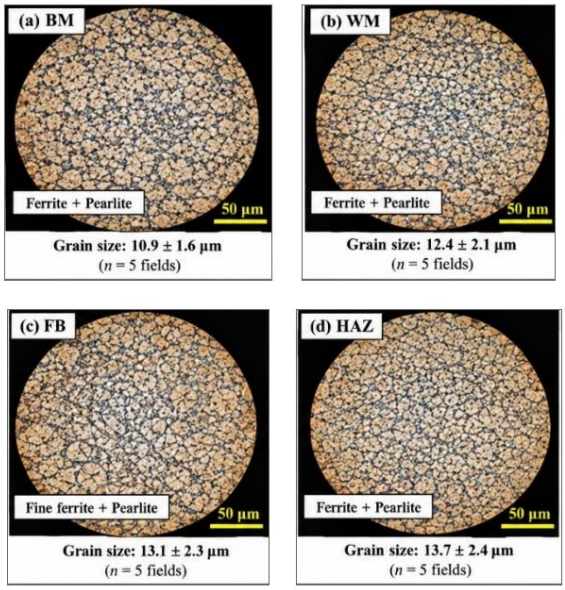


Fig. 5. Optical microstructures of SS400 steel welded at 70 A and 4 mm/s (nominal HI = 0.363 kJ/mm): (a) BM, (b) WM, (c) FB and (d) HAZ. Reported HAZ grain size: 13.7 ± 2.4 μm (n = 5 fields); scale bars are retained from the supplied micrographs.

The lower-input condition combines a smaller reported mean HAZ grain size (13.7 versus 20.3 μm) with a higher UTS mean (+53.4 MPa) and hardness

(+29.0 HV). This is consistent with a structure–property relationship, although a causal contribution from grain refinement cannot be isolated from changes in weld geometry or other microstructural features. The Hall–Petch relationship does not, by itself, support assignment of a specific 15–18 HV change.

4.4 Two-Way ANOVA Results (27 Specimens)

Tables 2 and 3 present two-way fixed-factor ANOVA results recalculated from the 27 specimen-level measurements. Factor degrees of freedom are 2 for current, 2 for speed, 4 for their interaction and 18 for within-cell error. The earlier inconsistent sums of squares and F-statistics have been replaced.

Table 2. Two-way ANOVA for UTS (MPa^2; n = 27).

Source	df	SS	MS	F	p
Current	2	2018.66	1009.33	5.75	0.01175
Speed	2	3419.66	1709.83	9.73	0.00136
I × v	4	615.20	153.80	0.88	0.49785
Error	18	3162.02	175.67	-	-
Total	26	9215.54	-	-	-

Table 3. Two-way ANOVA for HAZ hardness (HV^2; n = 27).

Source	df	SS	MS	F	p
Current	2	578.01	289.00	8.68	0.00229
Speed	2	1329.21	664.60	19.96	0.00003
I × v	4	17.39	4.35	0.13	0.96920
Error	18	599.26	33.29	-	-
Total	26	2523.87	-	-	-

For UTS, current yielded $F(2,18) = 5.75$ ($p = 0.0118$), speed $F(2,18) = 9.73$ ($p = 0.00136$), and their interaction $F(4,18) = 0.88$ ($p = 0.498$). For hardness, the corresponding values were $F(2,18) = 8.68$ ($p = 0.00229$), $F(2,18) = 19.96$ ($p = 0.0000270$), and $F(4,18) = 0.13$ ($p = 0.969$). Travel speed accounted for a greater factorial sum of squares than current for both responses, within these tested factor levels. A non-significant interaction does not establish that the effects are perfectly independent.

ANOVA diagnostic checks showed non-normal full-model residuals for UTS (Shapiro–Wilk $p = 0.0144$) and hardness ($p = 0.00062$). A median-centred Levene test across the nine settings did not indicate unequal variances ($p > 0.99$ for both responses). Because each cell has only three specimens, the significant normality departures and small replication count limit robustness of the nominal F-test inferences. These results should be treated as exploratory and confirmed with additional independently produced specimens or a prespecified robust analysis.

4.5 Multiple Linear Regression for UTS

To eliminate the discrepancy between the previous regression predictions and the observed data, an additive ordinary least-squares model was fitted to all 27 specimen-level UTS records using current and speed as predictors. Nominal heat input was not entered again as an additional independent predictor because it was calculated from the same parameters at constant voltage and efficiency.

$$\text{UTS (MPa)} = 459.583 - 1.05833I + 13.78333v. \quad (2)$$

The current coefficient is −1.058 MPa/A and the speed coefficient is +13.783 MPa per mm/s. The nominal regression p-values are 0.00152 and 0.00010, respectively, but formal p-value interpretation should account for the significant residual non-normality.

Table 4. UTS regression coefficients fitted to all 27 specimen-level observations (ordinary least squares).

Predictor	Estimate	Std. error	t	p
Intercept	459.583	25.388	18.10	<0.00001
Current (A)	-1.058	0.296	-3.58	0.00152
Speed (mm/s)	13.783	2.958	4.66	0.00010

For 27 specimens, the additive regression gives $R^2 = 0.590$, adjusted $R^2 = 0.556$ and residual standard error of 12.55 MPa (24 residual degrees of freedom). Figure 6 shows predicted against actual UTS using the correct MPa range. Regression residuals were non-normal by the Shapiro–Wilk test ($p = 0.0070$); no independent validation dataset was used. A larger R^2 calculated from the nine condition means would discard within-setting variation.

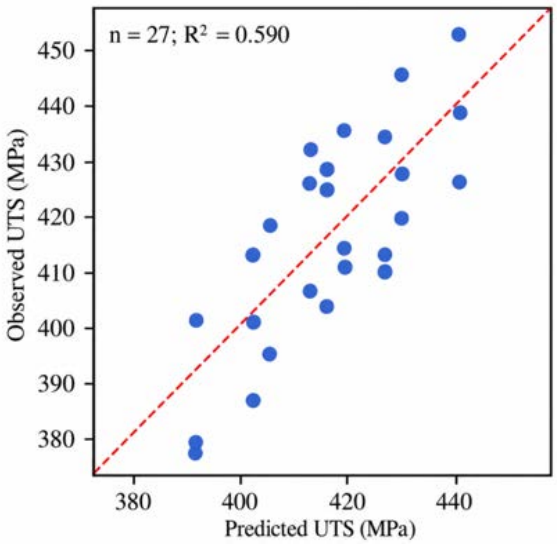


Fig. 6. Observed versus fitted UTS for the 27 tensile specimens from Equation (2) ($R^2 = 0.590$). Dashed line: perfect agreement.

At 90 A/2 mm/s, Equation (2) predicts approximately 391.9 MPa, compared with the observed cell mean of 385.8 MPa; this resolves the earlier prediction inconsistency. Because the regression was

assessed in-sample and residual normality was not satisfied, its coefficients are reported as descriptive within the investigated parameter space, not as a validated industrial prediction tool.

4.6 Best Observed Settings and Practical Boundaries

Among the nine experimental combinations, the highest mean UTS and HAZ hardness were achieved at 70 A/4 mm/s (439.2 MPa and 187.0 HV; nominal HI = 0.363 kJ/mm). The combinations 70 A/3 mm/s and 80 A/4 mm/s also attained mean UTS ≥ 419 MPa and HAZ hardness ≥ 180 HV. These are the best observed settings, not a qualified process window: independent production replicates, weld integrity requirements and service-specific performance tests must be considered before application.

5 Conclusion

The effects of current (70–90 A) and travel speed (2–4 mm/s) on SMAW joints in SS400 steel were evaluated using 27 individual tensile and HAZ-hardness measurements, supplemented by the author-supplied optical microstructure results. The principal conclusions are:

1. The corrected nominal effective heat-input range is 0.363–0.934 kJ/mm at V = 25 V and $\eta = 0.83$. The best-observed setting was 70 A/4 mm/s, with 439.2 ± 13.3 MPa UTS and 187.0 ± 5.7 HV hardness; the 90 A/2 mm/s setting gave 385.8 ± 13.3 MPa and 158.0 ± 5.7 HV. The difference in hardness is 29.0 HV (18.4%).
2. In nominal two-way ANOVA, both current and speed were associated with UTS ($p = 0.0118$ and 0.00136) and hardness ($p = 0.00229$ and 0.000027). Neither interaction was detected ($p = 0.498$ and 0.969), although residual normality departures require cautious interpretation of the F-test p-values.
3. The supplied microstructure annotations indicate finer HAZ grains at the lowest nominal input (13.7 ± 2.4 µm, n = 5 fields) compared with the highest-input condition (20.3 ± 3.1 µm, n = 5 fields), consistent with the tensile and hardness trends. These field-summary statistics should not be interpreted as independent specimen-level replication.
4. Regression of the 27 UTS observations yielded UTS (MPa) = 459.583 − 1.05833I + 13.78333v, with $R^2 = 0.590$ (adjusted $R^2 = 0.556$). This equation is descriptive over the experimental factor ranges; external predictive validation has not been performed.
5. The 70 A/4 mm/s combination provides the most favourable observed mechanical responses in the investigated matrix. Its application in fabrication should be subject to procedure qualification, defect control and testing relevant to the intended service conditions.

Future work should investigate field-to-field and specimen-to-specimen microstructural variation, validate the regression with independently produced joints, and evaluate fracture location, impact toughness and fatigue performance.

6 Acknowledgements

The authors acknowledge the technical support of the Mechanical Engineering Laboratory, Politeknik Industri Logam Morowali, and the Faculty of Engineering, Universitas Negeri Surabaya. The authors report no external funding for this work.

References

[1] R. Conte, F. R. Battista, G. Ambrogio, Submerged arc welding process: enhancement of production performance based on metallurgical observations. Int. J. Adv. Manuf. Technol. 134, 781–793 (2024). https://doi.org/10.1007/s00170-024-14153-y

[2] P.K. Baghel, Effect of SMAW process parameters on similar and dissimilar metal welds: An overview. Heliyon 8(12), e12161 (2022). https://doi.org/10.1016/j.heliyon.2022.e12161

[3] J. Singh, G. Singh, Effects of variation in welding current during SMAW process on A36 mild steel. Int. J. Res. Appl. Sci. Eng. Technol. 10(8), 259–264 (2022). https://doi.org/10.22214/ijraset.2022.46148

[4] M.S. Afzal, A. Wakeel, M.A. Nasir, M.I. Qazi, M. Abas, Optimization of process parameters for SMAW of ASTM A572 grade 50. J. Eng. Res. (2024). https://doi.org/10.1016/j.jer.2024.01.005

[5] T. Tarmizi, Y. B. Nugraha, I. Irfan, Analysis of current on mechanical properties and microstructure of A53 Gr B material with gas tungsten arc welding process. TEKNIK 42(1), 20–28 (2021). https://doi.org/10.14710/teknik.v42i1.33209

[6] H. Wibowo, M. N. Ilman, P. T. Iswanto, Analisa heat input pengelasan terhadap distorsi, struktur mikro dan kekuatan mekanis baja A36. Jurnal Rekayasa Mesin 7(1), 5–12 (2016). https://doi.org/10.21776/ub.jrm.2016.007.01.2

[7] A. Royani, Pengaruh suhu terhadap laju korosi baja karbon rendah dalam media air laut. Jurnal Simetrik 10(2), 344–349 (2020; published online 2021). https://doi.org/10.31959/js.v10i2.493

[8] R. Celin, J. Burja, Effect of cooling rates on the weld heat affected zone coarse grain microstructure. Metall. Mater. Eng. 24(1), 37–44 (2018). https://doi.org/10.30544/342

[9] Azwinur, Syukran, Hamdani, Kaji sifat mekanik sambungan las butt weld dan double lap joint pada material baja karbon rendah. SINTEK 12(1), 9–16 (2018). https://doi.org/10.24853/sintek.12.1.9-16

[10] H. Helanianto, E. Epriyandi, H. Rahmadi, Pengaruh variasi arus pengelasan SMAW terhadap kekerasan logam induk dan logam las. ELEMEN

7(2), 138–147 (2020). https://doi.org/10.34128/je.v7i2.148
[11] D. Ary, N. Muhayat, T. Triyono, Research gap finding in shielded metal arc welding of steel. E3S Web Conf. 465, 01012 (2023). https://doi.org/10.1051/e3sconf/202346501012
[12] C. Johan, M. Pineng, M. Pakiding, Analisis kekuatan bending hasil pengelasan SMAW pada baja ST 42 menggunakan pendingin oli SAE 20W-50 dengan memvariasi kuat arus. J. Teknik Industri 9(2), 390 (2023). https://doi.org/10.24014/jti.v9i1.22989
[13] M. A. Shomad, M. Shahar Mushfi, Analisis pengaruh variasi elektroda las E6013 dan E7018 terhadap kekuatan tarik dan kekerasan pada bahan baja SS 400. Dinamika Teknik Mesin 7(2), 73–79 (2017). https://doi.org/10.29303/d.v7i2.156
[14] S. Dharma, S. Suherman, S. Sarjianto, R. Sebayang, H. B. Kurniyanto, Pengaruh kuat arus terhadap sifat mekanis pada aluminium Al-Si-Fe dengan filler ER 4043 metode pengelasan GTAW. Jurnal Rekayasa Mesin 17(1), 103–112 (2022). https://doi.org/10.32497/jrm.v17i1.3068
[15] A. Widyianto, A. Yudianto, H. Sofyan, G. Gunadi, Karakterisasi kualitas lasan pada bahan serupa AZ31B dengan proses micro-friction stir spot welding (μFSSW) untuk aplikasi kendaraan. J. Pendidikan Vokasi Otomotif 5(2), 101–118 (2023). https://doi.org/10.21831/jpvo.v5i2.60132
[16] A. S. Nurrohkayati, D. Zulrahman, S. Syach, M. Khairul, Welding quality engineering using the design of experiment method (Taguchi's method). Procedia Eng. Life Sci. 1(1) (2021). https://doi.org/10.21070/pels.v1i1.882
[17] P. Kusdiyarto, R. D. Djatmiko, Analisis variasi included angle terhadap distorsi pada sambungan las SMAW. J. Dinamika Vokasional Teknik Mesin 3(1), 12–18 (2018). https://doi.org/10.21831/dinamika.v3i1.19112
[18] V. K. Kumawat, Performance analysis of welded joint made by MIG welding process on EN-24 steel work pieces for micro hardness. Int. J. Res. Appl. Sci. Eng. Technol. 7(5), 763–770 (2019). https://doi.org/10.22214/ijraset.2019.5128
[19] M. D. Jagtap, A review on optimization of welding process using different statistical techniques. Int. J. Res. Appl. Sci. Eng. Technol. 6(4), 2097–2100 (2018). https://doi.org/10.22214/ijraset.2018.4359
[20] S. Park, M. Choi, D. Kim, C. Kim, N. Kang, Modeling yield strength of austenitic stainless steel welds using multiple regression analysis and machine learning. Metals 13(9), 1625 (2023). https://doi.org/10.3390/met13091625
[21] S. Nugraha, H. Oktadinata, Pengaruh metode pengelasan TIG dan SMAW terhadap sifat mekanik baja karbon SS400. J. Ilmiah Teknik Mesin 10(1), 37 (2022). https://doi.org/10.33558/jitm.v10i1.2947
[22] C. Umam, U. Sukamto, Pengaruh variasi kuat arus pengelasan terhadap berat deposit las per milimeter. J. Metallurgical Eng. Process. Technol. 3(2), 159 (2023). https://doi.org/10.31315/jmept.v3i2.6584
[23] M.A. Shaleh, W. Wijoyo, R. Rohmadi, Pengaruh variasi metal transfer terhadap karakteristik sambungan las GMAW. J. Metallurgical Eng. Process. Technol. 3(2), 139 (2023). https://doi.org/10.31315/jmept.v3i2.8764
[24] S. Muddin, Ariyanto, Sriwati, M. F. Rahman, Optimization of welding direction model parameters to enhance the tensile strength of ST 42 steel joints through variation of current strength simulation. Eastern-European J. Enterprise Technol. 2(12[128]), 23–31 (2024). https://doi.org/10.15587/1729-4061.2024.295536
[25] A. Jefiza, D. Diono, S. Lukito, Analisis data monitoring proses pengelasan FCAW berbasis multilayer perceptron. J. Integrasi 14(2), 153–158 (2022). https://doi.org/10.30871/ji.v14i2.4538
[26] British Standards Institution, BS EN 1011-1:2009: Welding. Recommendations for welding of metallic materials. General guidance for arc welding (2009). https://doi.org/10.3403/30158904
[27] International Organization for Standardization, ISO 18491:2026, Welding and allied processes—Measurement of arc energies (2026). https://www.iso.org/standard/88807.html
[28] ASTM International, ASTM E112-24, Standard test methods for determining average grain size (2024). https://store.astm.org/e0112-24.html